

# Configuration Comparison for Surgical Robotic Systems Using a Single Access Port and Continuum Mechanisms

Kai Xu\*, *Member, IEEE* and Xidian Zheng, *Student Member, IEEE*

**Abstract**—Research on robot-assisted laparoscopic SPA (Single Port Access) surgery and N.O.T.E.S (Natural Orifice Transluminal Endoscopic Surgery) have thrived in the past a few years. A configuration similarity between these surgical robotic slaves is that two robotic arms are extended from the same access port (either a laparoscope or an endoscope) for surgical interventions. However, upon designing such a surgical robotic slave, the structure of the extended robotic arms has not been explored thoroughly based on evaluation of their distal dexterity. This paper presents a simulation-based comparison among three different structures which could be used to form these extended robotic arms. Results presented in this paper could serve as a design reference for surgical robotic slaves which use a single access port and continuum mechanisms.

## I. INTRODUCTION

SPA (Single Port Access) surgery uses one skin incision for laparoscopic interventions [1], while N.O.T.E.S (Natural Orifice Transluminal Endoscopic Surgery) only uses patients' natural orifices (such as vagina, GI track, etc.) for surgical treatments [2, 3]. Both procedures drew quite a bit of attention in the past a few years because of their potentials in further reducing postoperative complications to traditional laparoscopic MIS (Minimally Invasive Surgery) [4-6]. Looking at the promising future of the SPA and the N.O.T.E.S surgeries, robotics researchers constructed various robotic systems to assist the SPA surgeries [7-10] and the N.O.T.E.S procedures [11-13].

Surgical robotic systems for SPA surgeries usually use a straight and rigid laparoscope to access the surgical site through one skin incision, while those for N.O.T.E.S surgeries often use a flexible endoscope for access. The robot-assisted laryngeal MIS robotic system [14] could also fall in this category because a laryngoscope is used for access of the surgical site. A similarity among these surgical robotic systems is that two robotic arms will be extended from the same access port (laparoscope, endoscope or laryngoscope) to perform surgical tasks. Two examples are shown in Fig. 1, which are the IREP robot for SPA surgeries designed by Xu *et al* [7, 10] and the N.O.T.E.S surgical robot designed by Abbott *et al* [12].

Manuscript received Sept 15th, 2011. This work is supported by Shanghai Pujiang Scholar Program #11PJ1405600.

Kai Xu is with University of Michigan - Shanghai Jiao Tong University Joint Institute, Shanghai Jiao Tong University, Shanghai, 200240, China (corresponding author, phone: 86-21-34207220; fax: 86-21-34206525; email: [k.xu@sjtu.edu.cn](mailto:k.xu@sjtu.edu.cn))

Xidian Zheng is with the University of Michigan - Shanghai Jiao Tong University Joint Institute, Shanghai Jiao Tong University, Shanghai, 200240, China (email: [xdzheng@sjtu.edu.cn](mailto:xdzheng@sjtu.edu.cn)).

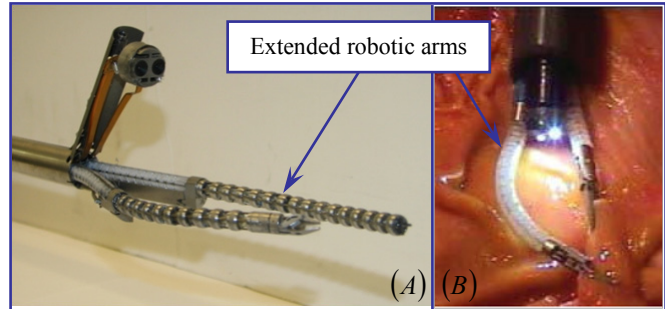


Fig. 1. Surgical robotic slaves which use one access port: (A) the IREP robot for SPA surgeries as in [7, 10], and (B) the N.O.T.E.S surgical robot as in [12]. In order to provide a design guide for structure of the systems' extended robotic arms, this paper presents a comparison for distal dexterity among different robotic arms.

Upon designing robotic slaves for the SPA and the N.O.T.E.S surgeries, attention was often primarily paid to satisfy the demanding geometrical constraints in order to fit everything into one laparoscope or endoscope. Structure of the systems' robotic arms has not been explored thoroughly based on the evaluation of their distal dexterity. A comparison for distal dexterity among different structures of these robotic arms is missing from the existing literature.

The contribution of this paper lies on the evaluation of distal dexterity for three robotic arms with different structures. Results of this comparison could provide a quantitative design reference for surgical robotic systems for the SPA or the N.O.T.E.S surgeries. Since the surgical robotic slave using continuum mechanisms for SPA surgeries [7, 10] had a smaller outer diameter than those using rigid articulated links [8, 9] ( $\varnothing 15\text{mm}$  vs  $\varnothing 23\text{mm}$  and  $\varnothing 30\text{mm}$  respectively) with comparable performance specifications, this paper chooses to focus on different structures using continuum mechanisms.

The paper is organized as follows. Section II presents the problem statement for the comparison among three different robotic arms. Section III presents modeling nomenclature while Section IV presents kinematics of each robotic arm. Simulation results are detailed and discussed in Section V with conclusion followed in Section VI.

## II. COMPARISON FORMULATION

In surgeries which use one access port (such as SPA surgeries and N.O.T.E.S surgeries shown in Fig. 1), two or more robotic arms will be extended from the shared access port for surgical interventions. Different structures of these extended robotic arms will lead to different distal dexterity and system performance. This paper presents a comparison for distal dexterity among three different robotic structures, which all use continuum mechanisms. The comparison results

are expected to provide a design reference for future development of such surgical robotic systems.

### A. Structure of the Compared Robotic Arms

In surgical robotic systems which use a single access port, the extended robotic arms had different number of DoFs (Degrees of Freedom): 5 DoFs as in [9], 6 DoFs as in [8], 7 DoFs as in [7, 10], and 8 DoFs as in [14]. In order to ensure a full 3D manipulation capability, this presented comparison assumes 7 DoFs for each robotic arm.

In Fig. 2, each robotic structure consists of two or three segments of continuum mechanisms as shown in Fig. 3. Each continuum segment consists of four super-elastic backbones and several disks, where one primary backbone is centrally located and is attached to the end disk. Three secondary backbones are equidistant from each other and from the primary backbone. The secondary backbones are attached to the end disk and can slide in holes of the base disk and the spacer disks. A 2-DoF bending motion of this continuum segment can be achieved through simultaneous actuation of the secondary backbones while keeping the length of the primary backbone constant. Length of the continuum segment is defined as the length of the primary backbone. A third DoF can be realized by actively changing the length of the primary backbone. Two or more segments can be stacked to form a robotic arm with more DoFs by using concentric tubes as the backbones. Structures to be compared which all have 7 DoFs are formed as follows, according to Fig. 2.

- **Structure A** has two 2-DoF continuum segments, a 2-DoF planar translational module, and a 1-DoF rotary wrist. In the 2-DoF continuum segments, length of the primary backbone remains constant.
- **Structure B** has three 2-DoF continuum segments and a 1-DoF rotary wrist.
- **Structure C** has two 3-DoF continuum segments and a 1-DoF rotary wrist. The third DoF of the continuum segment is realized by actively changing the length of the primary backbone.

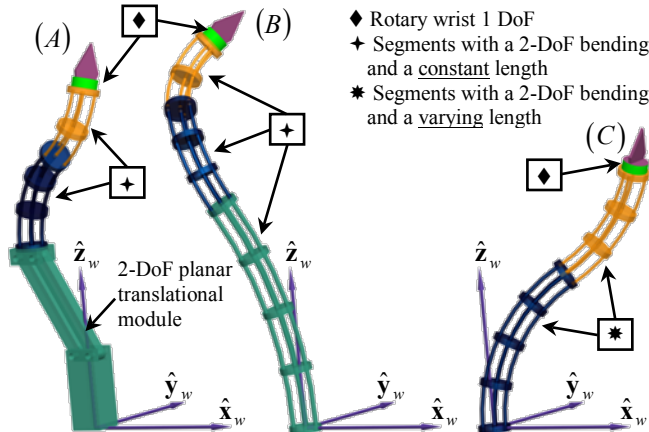


Fig. 2. Three 7-DoF structures are assumed for this comparison: (A) **Structure A** consists of two 2-DoF continuum segments, a 2-DoF planar translational module and a 1-DoF rotary wrist, (B) **Structure B** consists of three 2-DoF continuum segments and a 1-DoF rotary wrist, and (C) **Structure C** consists of two 3-DoF continuum segments that can actively change the length of the primary backbone.

### B. Evaluation of Distal Dexterity

Measure of dexterity or manipulability of a robot has been intensively studied [15-17]. Most measures involve different interpretation of singular values of the robot's Jacobian matrix with or without normalization, such as determinant, condition number, etc.

A Jacobian matrix represents mapping between velocities (or general actuation forces) in a robot's joint space and Euclidian velocities (or wrench) of the end effector. Unlike industrial robotic applications in which velocities, precision, stiffness, etc. are emphasized for higher productivity and efficiency, medical robots are designed towards different considerations such as safety, compactness, compliance and delicacy. Within a translational workspace which covers the targeted surgical site, surgeons are more concerned about whether they can orient tools and approach organs as desired. Speed of surgical manipulation is usually concerned secondarily and the manipulation speed can be relatively easily improved by using more powerful actuators.

The paper proposes to evaluate the distal dexterity of each robotic arm as the solid angle swept by the axis of the arm's gripper at selected points in the robot's workspace, as shown in Fig. 9, Fig. 10 and Fig. 11. These selected points are the vertices and the central point of a cube fitted in each arm's translational workspace. In other words, the distal dexterity is evaluated as a subset<sup>1</sup> of the orientation workspace at selected points for these robotic arms with their translational workspace enveloping the same functional volume.

In order to make the comparison more consistent, these robotic arms are predetermined to have the same reach (the furthest point along  $\hat{z}_w$  in Fig. 2 that can be reached). Dimension synthesis of each arm is performed such that the translational workspace envelops a same functional volume, as shown in Fig. 6, Fig. 7 and Fig. 8. The size of the functional volume is a cube of 50mm×50mm×50mm, which is required by a cholecystectomy according to [10, 18].

### III. MODELING NOMENCLATURE

All three structures in Fig. 2 use multiple continuum structures shown in Fig. 3. Since these segments are structurally similar, Fig. 3 only shows the  $t$ th segment ( $t=1, 2, \text{ or } 3$ ). Nomenclatures are defined in Table I, while coordinate systems of the  $t$ th segment are defined as below:

- **Base Disk Coordinate System (BDS)** is designated as  $\{tb\} \equiv \{\hat{x}_{tb}, \hat{y}_{tb}, \hat{z}_{tb}\}$ . It is attached to the base disk of the  $t$ th segment, whose XY plane coincides with the base disk and its origin is at the center of the base disk.  $\hat{x}_{tb}$  points from the center of the base disk to the first secondary backbone while  $\hat{z}_{tb}$  is perpendicular to the base disk. Secondary backbones are numbered according to the definition of  $\delta_{ti}$ .

<sup>1</sup> The orientation workspace includes a complete set of information of the gripper's orientation, where here only the direction of the gripper's axis is concerned (roll angle, rotation around its own axis, is not included).

- *Bending Plane Coordinate System 1* (BPS1) is designated as  $\{t1\} \equiv \{\hat{\mathbf{x}}_{t1}, \hat{\mathbf{y}}_{t1}, \hat{\mathbf{z}}_{t1}\}$  which shares its origin with  $\{tb\}$  and has the continuum segment bending in its XZ plane.
- *Bending Plane Coordinate System 2* (BPS2) is designated as  $\{t2\} \equiv \{\hat{\mathbf{x}}_{t2}, \hat{\mathbf{y}}_{t2}, \hat{\mathbf{z}}_{t2}\}$  obtained from  $\{t1\}$  by a rotation about  $\hat{\mathbf{y}}_{t1}$  such that  $\hat{\mathbf{z}}_{t2}$  becomes backbone tangent at the end disk. Origin of  $\{t2\}$  is at center of the end disk.
- *End Disk Coordinate System* (EDS)  $\{te\} \equiv \{\hat{\mathbf{x}}_{te}, \hat{\mathbf{y}}_{te}, \hat{\mathbf{z}}_{te}\}$  is fixed to the end disk of the  $t$ th segment.  $\hat{\mathbf{x}}_{te}$  points from center of the end disk to the first secondary backbone and  $\hat{\mathbf{z}}_{te}$  is normal to the end disk.  $\{te\}$  is obtained from  $\{t2\}$  by a rotation about  $\hat{\mathbf{z}}_{t2}$ .

When the  $t$ th and  $(t+1)$ th segment are stacked,  $\{te\}$  coincides with  $\{(t+1)b\}$ .

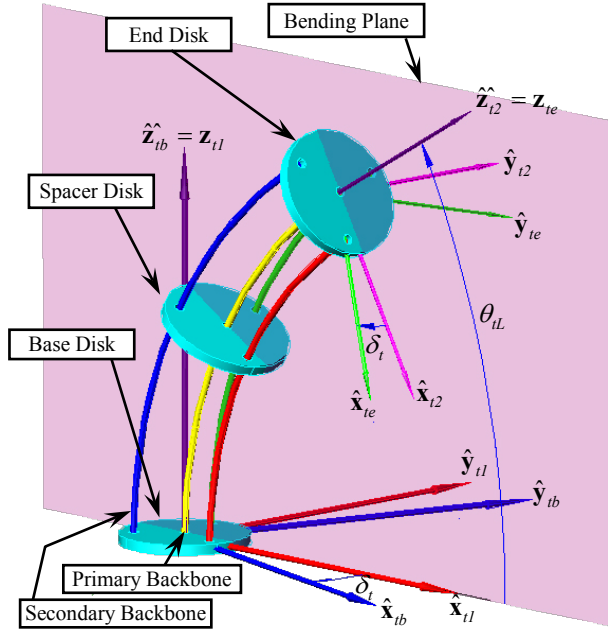


Fig. 3. Nomenclature and coordinates of the  $t$ th continuum segment

TABLE I  
NOMENCLATURE USED IN THIS PAPER

$i$	Index of the secondary backbones, $i = 1, 2, 3$
$t$	Index of the segments $t = 1, 2, \dots, n$ ; numbering of the segments always precedes the secondary backbones.
$r$	Radius of the pitch circle defining the positions of the secondary backbones in all the disks.
$\beta$	Division angle of the secondary backbones along the circumference of the pitch circle, $\beta = 2\pi/3$ .
$L_t, L_{ti}$	Length of the primary and the $i$ th secondary backbone for the $t$ th segment
$\mathbf{q}_t$	$\mathbf{q}_t = [q_{t1} \ q_{t2} \ q_{t3}]^T$ is the actuation length vector in the joint space for the $t$ th segment, where $q_{ti} \equiv L_{ti} - L_t$ .
$\theta_t(s)$	The angle of the tangent to the primary backbone in the bending plane for the $t$ th segment. $\theta_t(L_t)$ and $\theta_t(0)$ are designated by $\theta_{tL}$ and $\theta_0$ . $\theta_0 = \pi/2$ is a constant.
$\delta_{ti}$	For the $t$ th segment, a right-handed rotation angle from $\hat{\mathbf{x}}_{t1}$ about $\hat{\mathbf{z}}_{t1}$ to a ray passing through the primary

	backbone and the $i$ th secondary backbone. At a straight configuration $\hat{\mathbf{x}}_{t1}$ is along the same direction as the desired instantaneous linear velocity of the end disk.
$\delta_t$	$\delta_t \equiv \delta_{t1}$ and $\delta_{ti} = \delta_t + (i-1)\beta$ , $i = 1, 2, 3$
$\Psi_t$	$\Psi_t = [\theta_{tL} \ \delta_t]^T$ is a configuration vector which defines the pose of the $t$ th segment.
${}^l\mathbf{R}_2$	Coordinate transformation matrix frame 2 to frame 1.
${}^{tb}\mathbf{p}_t(s)$	Position vector of a point along the primary backbone in $\{tb\}$ . ${}^{tb}\mathbf{p}_t(L_t)$ is the tip position designated by ${}^{tb}\mathbf{p}_{tL}$ .

#### IV. KINEMATICS

Thorough analysis of one continuum segment's kinematics can be found in [14, 19-22]. Related entities are summarized here for completeness. Kinematics of one segment will be used to assemble the kinematics of different structures.

##### A. Kinematics of the $t$ th Segment

Shape of the  $t$ th continuum segment can be characterized by  $\Psi_t = [\theta_{tL} \ \delta_t]^T$  as defined in Table I. The experimentally proven assumption that the segment bends into a circular shape [19] gives the following.

$${}^{tb}\mathbf{p}_{tL} = \frac{L_t}{\theta_{tL} - \theta_0} \begin{bmatrix} \cos \delta_t (\sin \theta_{tL} - 1) \\ \sin \delta_t (1 - \sin \theta_{tL}) \\ -\cos \theta_{tL} \end{bmatrix} \quad (1)$$

Where  ${}^{tb}\mathbf{p}_{tL} = [0 \ 0 \ L_t]^T$  when  $\theta_{tL} = \theta_0 = \pi/2$

Rotation matrix  ${}^{tb}\mathbf{R}_{te}$  associates  $\{te\}$  and  $\{tb\}$ .

$${}^{tb}\mathbf{R}_{te} = \mathbf{R}(\hat{\mathbf{z}}_{tb}, -\delta_t) \mathbf{R}(\hat{\mathbf{y}}_{t1}, \theta_0 - \theta_{tL}) \mathbf{R}(\hat{\mathbf{z}}_{t2}, \delta_t) \quad (2)$$

Where  $\mathbf{R}(\hat{\mathbf{n}}, \gamma)$  designates rotation about  $\hat{\mathbf{n}}$  by an angle  $\gamma$ .

The instantaneous kinematics is then given by:

$$\dot{\mathbf{x}}_t \Psi \mathbf{J}_{t\Psi}, \text{ where } \mathbf{J}_{t\Psi} = \begin{bmatrix} \mathbf{J}_{tV} \\ \mathbf{J}_{t\omega} \end{bmatrix} \quad (3)$$

$$\mathbf{J}_{tV} = \begin{bmatrix} L_t \cos \delta_t \frac{(\theta_{tL} - \theta_0) \cos \theta_{tL} - \sin \theta_{tL} + 1}{(\theta_{tL} - \theta_0)^2} & -L_t \frac{\sin \delta_t (\sin \theta_{tL} - 1)}{\theta_{tL} - \theta_0} \\ -L_t \sin \delta_t \frac{(\theta_{tL} - \theta_0) \cos \theta_{tL} - \sin \theta_{tL} + 1}{(\theta_{tL} - \theta_0)^2} & -L_t \frac{\cos \delta_t (\sin \theta_{tL} - 1)}{\theta_{tL} - \theta_0} \\ L_t \frac{(\theta_{tL} - \theta_0) \sin \theta_{tL} + \cos \theta_{tL}}{(\theta_{tL} - \theta_0)^2} & 0 \end{bmatrix} \quad (4)$$

$$\mathbf{J}_{t\omega} = \begin{bmatrix} -\sin \delta_t & \cos \delta_t \cos \theta_{tL} \\ -\cos \delta_t & -\sin \delta_t \cos \theta_{tL} \\ 0 & -1 + \sin \theta_{tL} \end{bmatrix}$$

Singularity of  $\mathbf{J}_{t\Psi}$  for  $\theta_{tL} = \theta_0 = \pi/2$  can be resolved as:

$$\lim_{\theta_{tL} \rightarrow \theta_0 = \pi/2} \mathbf{J}_{t\Psi} = \begin{bmatrix} -L_t \cos \delta_t / 2 & 0 \\ L_t \sin \delta_t / 2 & 0 \\ 0 & 0 \\ -\sin \delta_t & 0 \\ -\cos \delta_t & 0 \\ 0 & 0 \end{bmatrix} \quad (5)$$

##### B. Kinematics of Structure A

Robotic arms which use Structure A were adopted in the

IREP robot for SPA surgery [7, 10], as shown in Fig. 4. In the world coordinate system  $\{w\} \equiv \{\hat{x}_w, \hat{y}_w, \hat{z}_w\}$ , Structure A consists of the following:

1. Link A which provides a translation  $z$  along  $\hat{z}_w$
2. Linkage B with a length of  $h=35mm$  which connects to Link A via revolute joints and opens to an angle of  $\zeta$ .
3. Continuum segment 1 with coordinates systems through  $\{1b\}$  to  $\{1e\}$ , referring to Fig. 3. Linkage B is formed using parallelogram so that  $\{1b\}$  is parallel to  $\{w\}$ .
4. Continuum segment 2 with coordinates systems through  $\{2b\}$  to  $\{2e\}$ .  $\{1e\}$  coincides with  $\{2b\}$ .
5. A gripper with a coordinate system  $\{g\} \equiv \{\hat{x}_g, \hat{y}_g, \hat{z}_g\}$  attached.  $\{g\}$  is obtained from  $\{2e\}$  by a rotation of  $\phi$ .

The gripper tip in  $\{g\}$  is defined as  ${}^g\mathbf{p}_g = [0 \ 0 \ 15mm]^T$ .

Actual realization of this structure was detailed in [10]. A configuration vector  $\xi_{\Psi\Psi}[\phi \ \frac{T}{2} \ \frac{T}{1} \ \zeta \ z]^T$  can be defined for kinematics parameterization. Tip position and Jacobian of the gripper in  $\{w\}$  can be derived as the following with details available in [7].

$${}^w\mathbf{p}_g = {}^w\mathbf{p}_{1b} + {}^{1b}\mathbf{p}_{1L} + {}^{1b}\mathbf{R}_{1e} \left( {}^{2b}\mathbf{p}_{2L} + {}^{2b}\mathbf{R}_g {}^g\mathbf{p}_g \right) \quad (6)$$

Where  ${}^w\mathbf{p}_{1b} = z\hat{z}_w + h \cos \zeta \hat{x}_w + h \sin \zeta \hat{z}_w$ ,  ${}^{2b}\mathbf{R}_g = {}^{2b}\mathbf{R}_{2e} {}^{2e}\mathbf{R}_g$ ; the general expression for  ${}^{1b}\mathbf{p}_{1L}$  and  ${}^{2b}\mathbf{p}_{2L}$  are from Eq. (1).

$${}^w\dot{\mathbf{x}} = \xi \mathbf{J}_A \dot{\mathbf{A}} \quad (7)$$

$$\mathbf{J}_A = \begin{bmatrix} \mathbf{0}_{3 \times 1} & {}^{1b}\mathbf{R}_{2b} \mathbf{T}_{A2} & \mathbf{T}_{A1} & \mathbf{t}_A & \hat{z}_w \\ {}^{1b}\mathbf{R}_g \hat{z}_g & {}^{1b}\mathbf{R}_{2b} \mathbf{J}_{2\omega\omega} & \mathbf{J}_1 & \mathbf{0}_{3 \times 1} & \mathbf{0}_{3 \times 1} \end{bmatrix} \quad (8)$$

Where  ${}^{1b}\mathbf{R}_g = {}^{1b}\mathbf{R}_{2b} {}^{2b}\mathbf{R}_g$ ;  $\mathbf{T}_{A2}$ ,  $\mathbf{T}_{A1}$ , and  $\mathbf{t}_A$  are written below:

$$\mathbf{T}_{A2} = \mathbf{J}_{2\nu\omega} \left[ {}^{2b}\mathbf{R}_g {}^g\mathbf{p}_g \right]^\times \mathbf{J}_2 \quad (9)$$

$$\mathbf{T}_{A1} = \mathbf{J}_{1\nu\omega} \left[ {}^{1b}\mathbf{R}_{2b} {}^{2b}\mathbf{p}_{2L} + {}^{1b}\mathbf{R}_g {}^g\mathbf{p}_g \right]^\times \mathbf{J}_1 \quad (10)$$

$$\mathbf{t}_A = \frac{\partial}{\partial \zeta} ({}^w\mathbf{p}_{1b}) = -h \sin \zeta \hat{x}_w + h \cos \zeta \hat{z}_w \quad (11)$$

Where  $[\mathbf{p}]^\times$  is the skew-symmetric matrix of a vector  $\mathbf{p}$ . Expressions of  $\mathbf{J}_{1\nu}$ ,  $\mathbf{J}_{1\omega}$ ,  $\mathbf{J}_{2\nu}$  and  $\mathbf{J}_{2\omega}$  are from Eq. (4).

### C. Kinematics of Structure B

A robotic arm which uses Structure B was tested for its force sensing capability [20], as shown in Fig. 4. In the world coordinate system  $\{w\}$ , Structure B consists of the following:

1. Continuum segment 1 to 3 are stacked with coordinates systems through  $\{1b\}$  to  $\{1e\}$ ,  $\{2b\}$  to  $\{2e\}$ , and  $\{3b\}$  to  $\{3e\}$  attached, referring to Fig. 3.  $\{1b\}$ ,  $\{1e\}$  and  $\{2e\}$  coincide with  $\{w\}$ ,  $\{2b\}$  and  $\{3b\}$  respectively.
2. A gripper with a coordinate system  $\{g\} \equiv \{\hat{x}_g, \hat{y}_g, \hat{z}_g\}$

attached.  $\{g\}$  is obtained from  $\{3e\}$  by a rotation of  $\phi$ .

The gripper tip in  $\{g\}$  is defined as  ${}^g\mathbf{p}_g = [0 \ 0 \ 15mm]^T$ .

A configuration vector  $\xi_{\Psi\Psi\Psi}[\phi \ \frac{T}{3} \ \frac{T}{2} \ \frac{T}{1}]^T$  can be defined for parameterization. Tip position and Jacobian of the gripper in  $\{w\}$  can be derived as the following with details available in [20].

$${}^w\mathbf{p}_g = {}^{1b}\mathbf{p}_{1L} + {}^{1b}\mathbf{R}_{2b} \left( {}^{2b}\mathbf{p}_{2L} + {}^{2b}\mathbf{R}_{3b} \left( {}^{3b}\mathbf{p}_{3L} + {}^{3b}\mathbf{R}_g {}^g\mathbf{p}_g \right) \right) \quad (12)$$

Where  ${}^{3b}\mathbf{R}_g = {}^{3b}\mathbf{R}_{3e} {}^{3e}\mathbf{R}_g$ ;  ${}^{1b}\mathbf{p}_{1L}$ ,  ${}^{2b}\mathbf{p}_{2L}$  and  ${}^{3b}\mathbf{p}_{3L}$  are from Eq. (1).

$${}^w\dot{\mathbf{x}} = \xi \mathbf{J}_B \dot{\mathbf{B}} \quad (13)$$

$$\mathbf{J}_B = \begin{bmatrix} \mathbf{0}_{3 \times 1} & {}^{1b}\mathbf{R}_{3b} \mathbf{T}_{B3} & {}^{1b}\mathbf{R}_{2b} \mathbf{T}_{B2} & \mathbf{T}_{B1} \\ {}^{1b}\mathbf{R}_{3b} & {}^{3b}\mathbf{R}_g \hat{z}_g & {}^{1b}\mathbf{R}_{3b} \mathbf{J}_{3\omega\omega\omega} & {}^{1b}\mathbf{R}_{2b} \mathbf{J}_2 & \mathbf{J}_1 \end{bmatrix} \quad (14)$$

Where  ${}^{1b}\mathbf{R}_{3b} = {}^{1b}\mathbf{R}_{2b} {}^{2b}\mathbf{R}_{3b}$ ,  ${}^{3b}\mathbf{R}_g = {}^{3b}\mathbf{R}_{3e} {}^{3e}\mathbf{R}_g$  and

${}^{1b}\mathbf{R}_g = {}^{1b}\mathbf{R}_{3b} {}^{3b}\mathbf{R}_g$ ;  $\mathbf{T}_{B3}$ ,  $\mathbf{T}_{B2}$ ,  $\mathbf{T}_{B1}$  are written as follows:

$$\mathbf{T}_{B3} = \mathbf{J}_{3\nu\omega} \left[ {}^{3b}\mathbf{R}_g {}^g\mathbf{p}_g \right]^\times \mathbf{J}_3 \quad (15)$$

$$\mathbf{T}_{B2} = \mathbf{J}_{2\nu\omega} \left[ {}^{2b}\mathbf{R}_{3b} {}^{3b}\mathbf{p}_{3L} + {}^{2b}\mathbf{R}_{3b} {}^{3b}\mathbf{R}_g {}^g\mathbf{p}_g \right]^\times \mathbf{J}_2 \quad (16)$$

$$\mathbf{T}_{B1} = \mathbf{J}_{1\nu\omega} \left[ {}^{1b}\mathbf{R}_{2b} {}^{2b}\mathbf{p}_{2L} + {}^{1b}\mathbf{R}_{3b} {}^{3b}\mathbf{p}_{3L} + {}^{1b}\mathbf{R}_g {}^g\mathbf{p}_g \right]^\times \mathbf{J}_1 \quad (17)$$

Where  $\mathbf{J}_{1\nu}$ ,  $\mathbf{J}_{1\omega}$ ,  $\mathbf{J}_{2\nu}$ ,  $\mathbf{J}_{2\omega}$ ,  $\mathbf{J}_{3\nu}$  and  $\mathbf{J}_{3\omega}$  are from Eq. (4).

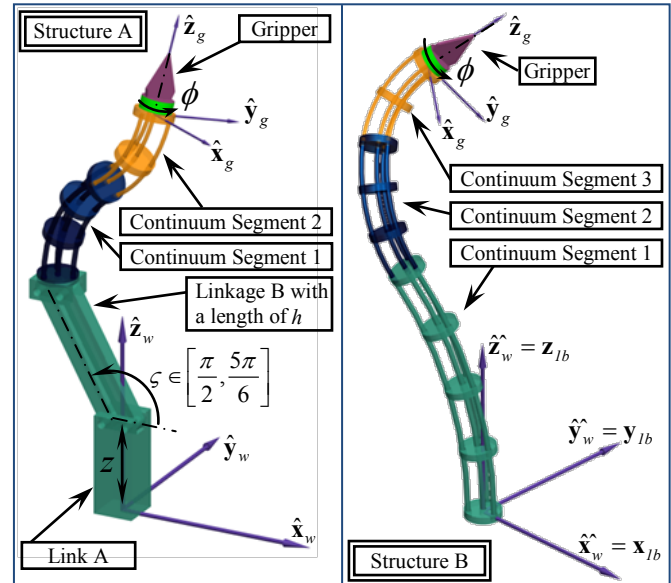


Fig. 4. Structure A and Structure B with the configuration vectors designed as  $\xi_{\Psi\Psi}[\phi \ \frac{T}{2} \ \frac{T}{1} \ \zeta \ z]^T$  and  $\xi_{\Psi\Psi\Psi}[\phi \ \frac{T}{3} \ \frac{T}{2} \ \frac{T}{1}]^T$  respectively.

### D. Kinematics of Structure C

In addition of Structure A and Structure B, performance of Structure C is explored in this paper, as shown in Fig. 5. In  $\{w\}$ , Structure C consists of the following:

1. Continuum segment 1 and 2 are stacked with coordinates systems through  $\{1b\}$  to  $\{1e\}$  and  $\{2b\}$  to  $\{2e\}$  attached, referring to Fig. 3.  $\{1b\}$  and  $\{1e\}$  coincide with  $\{w\}$  and

$\{2b\}$  respectively. Length of each segment now can be actively controlled to introduce an additional DoF.

2. A gripper with a coordinate system  $\{g\} \equiv \{\hat{x}_g, \hat{y}_g, \hat{z}_g\}$  attached.  $\{g\}$  is obtained from  $\{2e\}$  by a rotation of  $\phi$ .

The gripper tip in  $\{g\}$  is defined as  ${}^g \mathbf{p}_g = [0 \ 0 \ 15\text{mm}]^T$ .

A configuration vector  $\xi_{\Psi\Psi} [\phi \ \frac{\tau}{2} \ L_2 \ \frac{\tau}{1} \ L_1]^T$  can be defined for parameterization. Tip position of the gripper in  $\{w\}$  can be written as the following:

$${}^w \mathbf{p}_g = {}^{1b} \mathbf{p}_{1L} + {}^{1b} \mathbf{R}_{2b} \left( {}^{2b} \mathbf{p}_{2L} + {}^{2b} \mathbf{R}_{2e} {}^{2e} \mathbf{R}_g {}^g \mathbf{p}_g \right) \quad (18)$$

Where  ${}^{1b} \mathbf{p}_{1L}$  and  ${}^{2b} \mathbf{p}_{2L}$  are from Eq. (1).

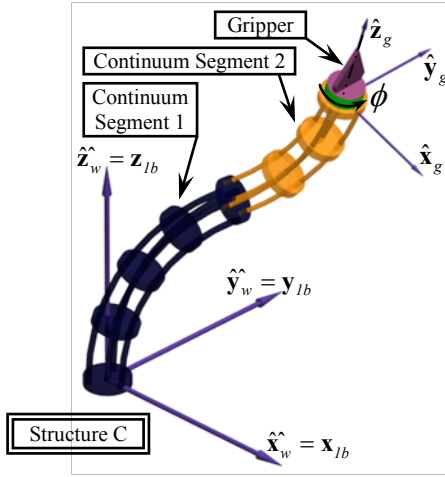


Fig. 5. Structure C with its configuration vector  $\xi_{\Psi\Psi} [\phi \ \frac{\tau}{2} \ L_2 \ \frac{\tau}{1} \ L_1]^T$

Jacobian matrix can be derived by writing linear velocity and angular velocity of the gripper as the following:

$${}^w \mathbf{v}_g = \mathbf{J}_1 \dot{\phi} + \mathbf{J}_2 \dot{L}_2 + \mathbf{J}_3 \dot{L}_1 + \mathbf{J}_4 \dot{\phi} + \mathbf{J}_5 \dot{L}_2 + \mathbf{J}_6 \dot{L}_1 \quad (19)$$

Where  ${}^{1b} \mathbf{R}_g = {}^{1b} \mathbf{R}_{2b} {}^{2b} \mathbf{R}_{2e} {}^{2e} \mathbf{R}_g$  and  ${}^{2b} \mathbf{R}_g = {}^{2b} \mathbf{R}_{2e} {}^{2e} \mathbf{R}_g$

$${}^w \boldsymbol{\omega}_g = \mathbf{J}_7 \dot{\phi} + \mathbf{J}_8 \dot{L}_2 + \mathbf{J}_9 \dot{L}_1 + \mathbf{J}_{10} \dot{\phi} + \mathbf{J}_{11} \dot{L}_2 + \mathbf{J}_{12} \dot{L}_1 \quad (20)$$

Then the Jacobian can be written as follows.

$$\dot{\mathbf{x}} = \mathbf{J}_C \dot{\xi} \quad (21)$$

$$\mathbf{J}_C = \begin{bmatrix} \mathbf{0}_{3 \times 1} & {}^{1b} \mathbf{R}_{2b} \mathbf{T}_{C2} & {}^{1b} \mathbf{R}_{2b} \mathbf{t}_{C2} & \mathbf{T}_{C1} & \mathbf{t}_{C1} \\ {}^{1b} \mathbf{R}_g \hat{\mathbf{z}}_g & {}^{1b} \mathbf{R}_{2b} \mathbf{J}_{2\omega\omega} & \mathbf{0}_{3 \times 1} & \mathbf{J}_1 & \mathbf{0}_{3 \times 1} \end{bmatrix} \quad (22)$$

Where  $\mathbf{T}_{C2}$ ,  $\mathbf{t}_{C2}$ ,  $\mathbf{T}_{C1}$  and  $\mathbf{t}_{C1}$  are written as below:

$$\mathbf{T}_{C2} = \mathbf{J}_{2\omega\omega} - [{}^{2b} \mathbf{R}_g {}^g \mathbf{p}_g]^\times \mathbf{J}_2 \quad (23)$$

$$\mathbf{t}_{C1} = \frac{[\cos \delta_i (\sin \theta_{iL} - 1) \sin \delta_i (1 - \sin \theta_{iL}) - \cos \theta_{iL}]^T}{\theta_{iL} - \theta_0} \quad (24)$$

For  $\mathbf{t}_{C1}$  and  $\mathbf{t}_{C2}$ ;  $\mathbf{t}_{C1} = [0 \ 0 \ 1]^T$  when  $\theta_{iL} = \theta_0 = \pi/2$

$$\mathbf{T}_{C1} = \mathbf{J}_{1\omega\omega} - [{}^{1b} \mathbf{R}_{2b} {}^{2b} \mathbf{p}_{2L} + {}^{1b} \mathbf{R}_g {}^g \mathbf{p}_g]^\times \mathbf{J}_1 \quad (25)$$

Where  $[\mathbf{p}]^\times$  is the skew-symmetric matrix of a vector  $\mathbf{p}$ . Expressions of  $\mathbf{J}_{1\omega}$ ,  $\mathbf{J}_{1\omega}$ ,  $\mathbf{J}_{2\omega}$  and  $\mathbf{J}_{2\omega}$  are from Eq. (4).

## V. SIMULATION RESULTS AND DISCUSSIONS

According to the kinematics of these structures derived in Section VI, translational workspace of these structures are generated to verify whether the desired functional volume (a cube of 50mm×50mm×50mm) is completely enveloped. In the actual implementation, multiple robotic arms will be extended from the same access port. Since the offsets between them are usually small, results shown here for one arm can easily transferred to a scenario where multiple arms are used.

The translational workspace of each structure in  $\{w\}$  is generated by scanning the configuration space, as plotted in Fig. 6, Fig. 7 and Fig. 8. Joints limits and structural constants of these structures are specified in Table II. For Structure A, all these values are consistent with the design presented in [7, 10]. To be noted, range of  $\zeta$  is not symmetric due to the difficulty of constructing such an actual linkage.

Position of the functional volume in Fig. 6 is slightly lower than that in Fig. 7 and Fig. 8 due to the specific shape of the translational workspace of Structure A.

TABLE II  
JOINT VARIABLES LIMITS AND STRUCTURAL CONSTANTS

For all the segments $\Psi_i = [\theta_{iL} \ \delta_i]^T$		$\theta_{iL} \in [0, \pi/2]$	$\delta_i \in [-\pi, \pi]$
Structure A	Configuration vector $\xi_{\Psi\Psi} [\phi \ \frac{\tau}{2} \ L_2 \ \frac{\tau}{1} \ \zeta \ z]^T$		
$\phi \in [-\pi, \pi]$	$L_1 = 35\text{mm}$	$L_2 = 25\text{mm}$	
$h = 35\text{mm}$	$\zeta \in [\pi/2, 5\pi/6]$		$z \in [15\text{mm}, 40\text{mm}]$
Structure B	Configuration vector $\xi_{\Psi\Psi} [\phi \ \frac{\tau}{3} \ \frac{\tau}{2} \ \frac{\tau}{1}]^T$		
$\phi \in [-\pi, \pi]$	$L_1 = 75\text{mm}$	$L_2 = 35\text{mm}$	$L_3 = 25\text{mm}$
Structure C	Configuration vector $\xi_{\Psi\Psi} [\phi \ \frac{\tau}{2} \ L_2 \ \frac{\tau}{1} \ L_1]^T$		
$\phi \in [-\pi, \pi]$	$L_2 \in [25\text{mm}, 55\text{mm}]$		$L_1 \in [35\text{mm}, 80\text{mm}]$

Distal dexterity of these structures at selected points (the vertices and the central point of the desired cube in the translational workspace) is evaluated as a solid angle swept by the axis of each structure's gripper.

The sweeping process is realized by using the pseudo inverse of each structure's Jacobian. Two steps are included:

1. From an initial configuration, each structure was driven to reach a selected point by a kinematics redundancy resolution (e.g. specify the linear velocity while minimizing angular velocity in certain directions).
2. At the selected point, each structure was driven to verify whether a direction could be reached by the gripper's axis.

The verification only concerns direction of the gripper's axis, because the gripper is connected to the continuum segment via a wrist which can rotate continuously. The verification was implemented as follows. A direction  $\hat{\mathbf{n}}_{xf}$  was first parameterized as a unit vector using two variables, an arbitrary unit vector  $\hat{\mathbf{n}}_{yf}$  which is normal to  $\hat{\mathbf{n}}_{xf}$  is picked

to form the desired orientation of the gripper. Because of the rotary wrist,  $\hat{n}_{xf}$  wouldn't affect the reachability of  $\hat{n}_{zf}$ .

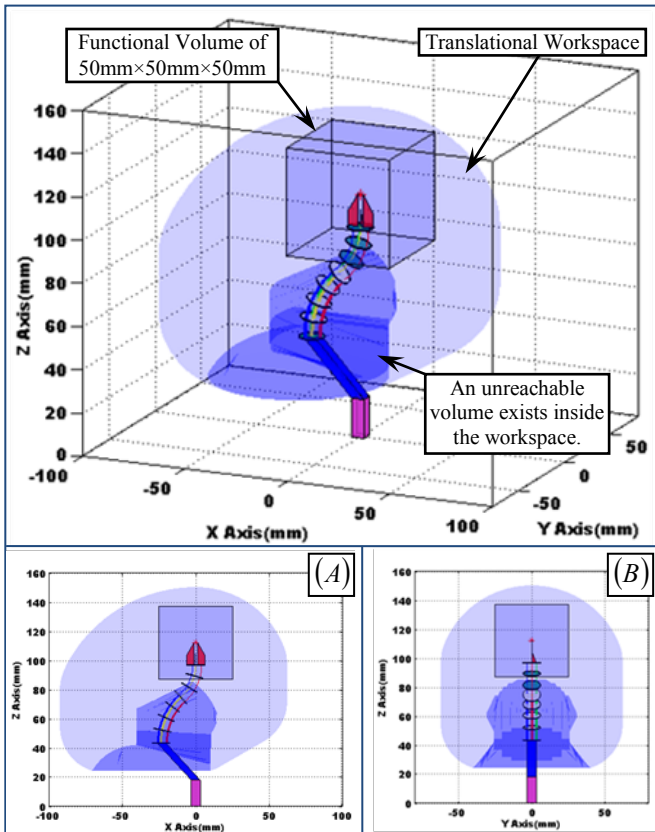


Fig. 6. Translational workspace of Structure A with specified joints limits as shown in Table II: (A) the front view and (B) the side view

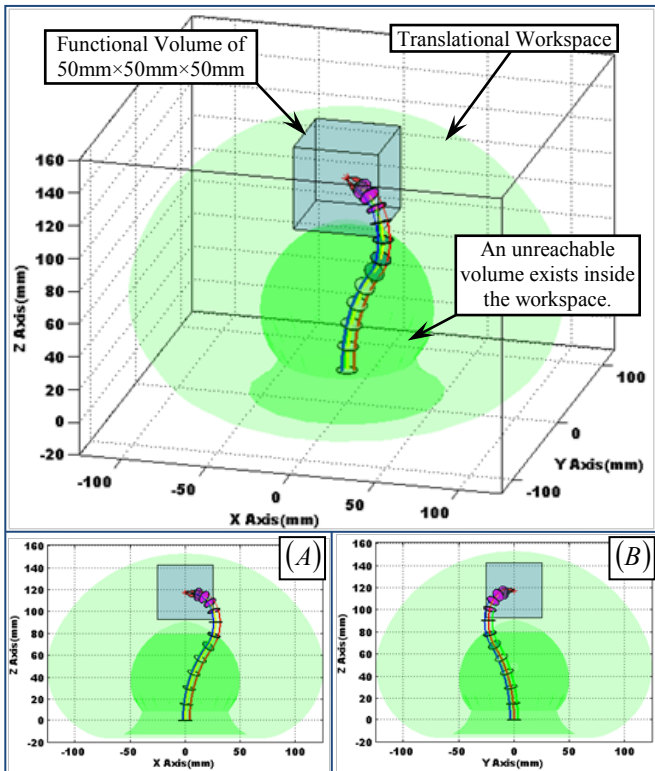


Fig. 7. Translational workspace of Structure B with specified joints limits as shown in Table II: (A) the front view and (B) the side view

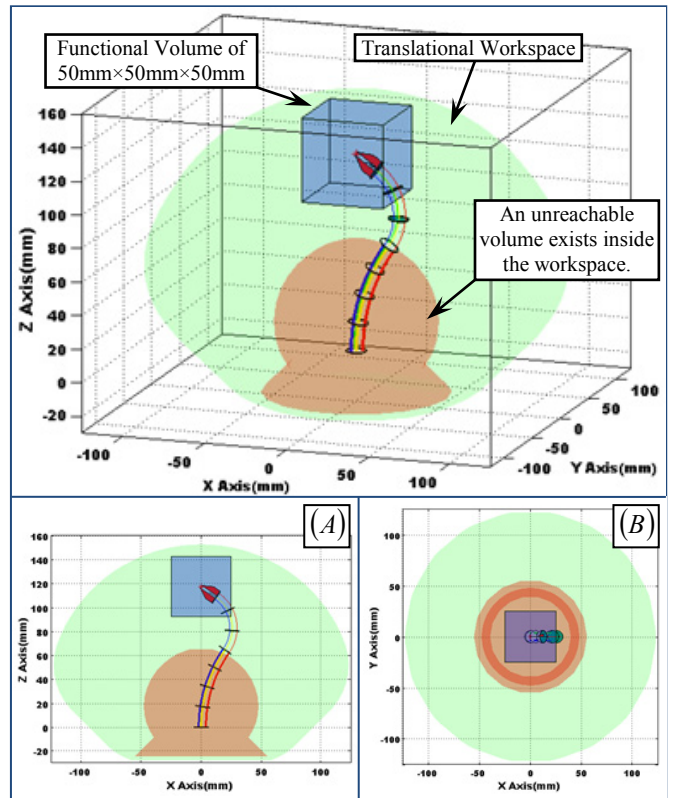


Fig. 8. Translational workspace of Structure C with specified joints limits as shown in Table II: (A) the front view and (B) the top view

Then each structure was driven by specifying a  $\dot{\mathbf{x}}$  which combines a linear velocity and an angular velocity, as shown in Eq.(26). The linear velocity always pointed towards the selected point. The angular velocity was generated from a rotation matrix associating the current orientation to the desired one. If a joint limit was reached first, this direction couldn't be reached and the next value for  $\hat{n}_{zf}$  would be verified. The process repeats itself till a fine parameterization of  $\hat{n}_{zf}$  is tested.

$$\dot{\xi} \mathbf{J} = (\dot{\mathbf{x}}_N)^+ \quad (26)$$

Where  $N = A, B$  or  $C$  as in Eq. (8), Eq.(14) and Eq.(22).

Each structure's distal dexterity is evaluated through a 2-dimensional numerical integral following the definition of a solid angle and the values are presented in Table III. Annotation of the points shown in Fig. 11(D) is identical for all the structures. The evaluated distal dexterity can be visualized as a patch on the surface of a sphere as in Fig. 9, Fig. 10 and Fig. 11. The attached multimedia extension shows simulations where the gripper's axis of each structure swept boundaries of the distal dexterity patches.

TABLE III  
DISTAL DEXTERITY EVALUATED FOR THE STRUCTURES (UNIT: STERADIAN)

Structure A	$P_1: 1.407$	$P_2: 1.470$	$P_3: 1.483$	$P_4: 1.395$
	$P_0: 2.023$	$P_5: 0.842$	$P_6: 0.842$	$P_7: 0.829$
Structure B	$P_1: 0.151$	$P_2: 0.138$	$P_3: 0.138$	$P_4: 0.138$
	$P_0: 2.815$	$P_5: 0.628$	$P_6: 0.641$	$P_7: 0.639$
Structure C	$P_1: 2.463$	$P_2: 2.458$	$P_3: 2.461$	$P_4: 2.460$
	$P_0: 2.727$	$P_5: 0.440$	$P_6: 0.415$	$P_7: 0.402$

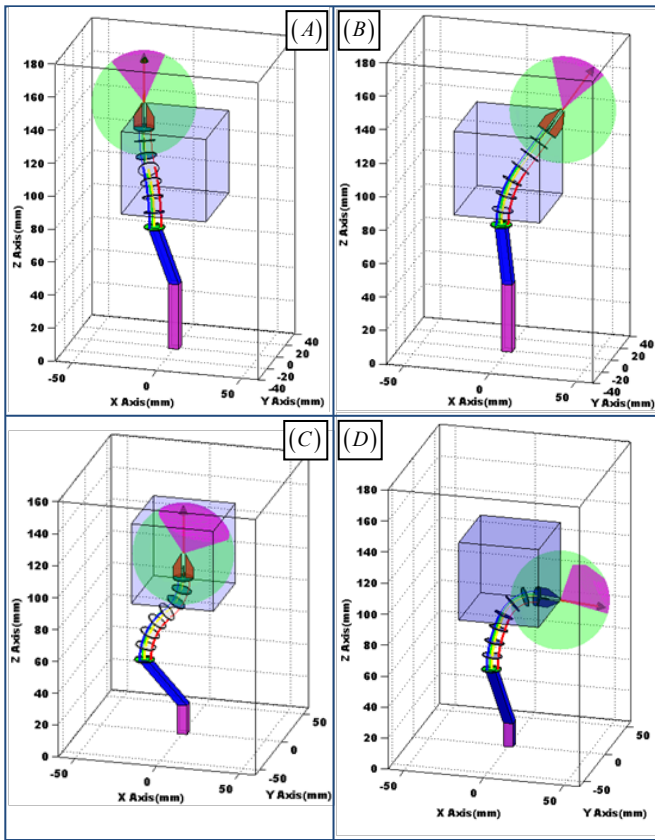


Fig. 9. Distal dexterity evaluated at selected points for Structure A: (A) at  $P_6$  point, (B) at  $P_5$  point, (C) at  $P_0$  point and (D) at  $P_1$  point.

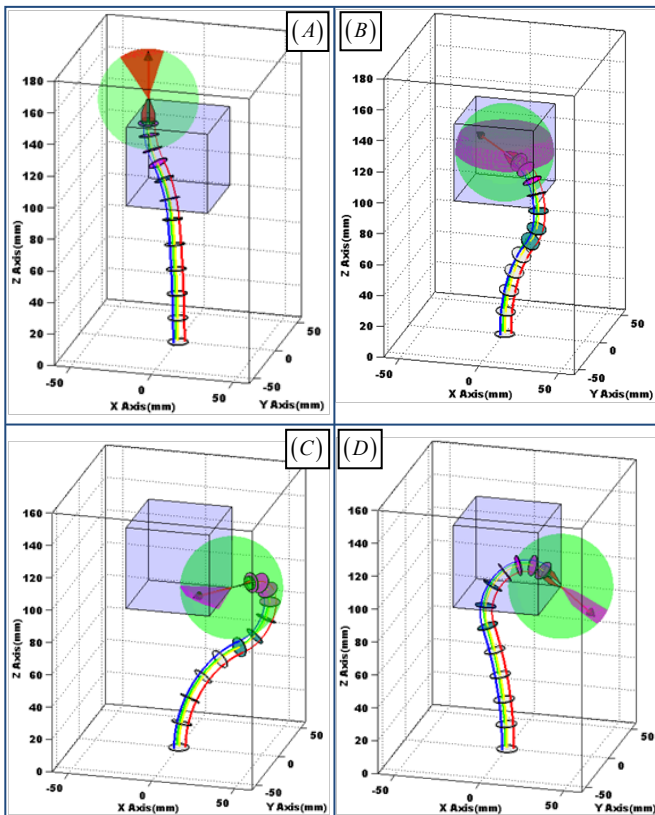


Fig. 10. Distal dexterity evaluated at selected points for Structure B: (A) at  $P_6$  point, (B) at  $P_0$  point, (C) at  $P_1$  point pointing inwards, and (D) at  $P_1$  point pointing outwards.

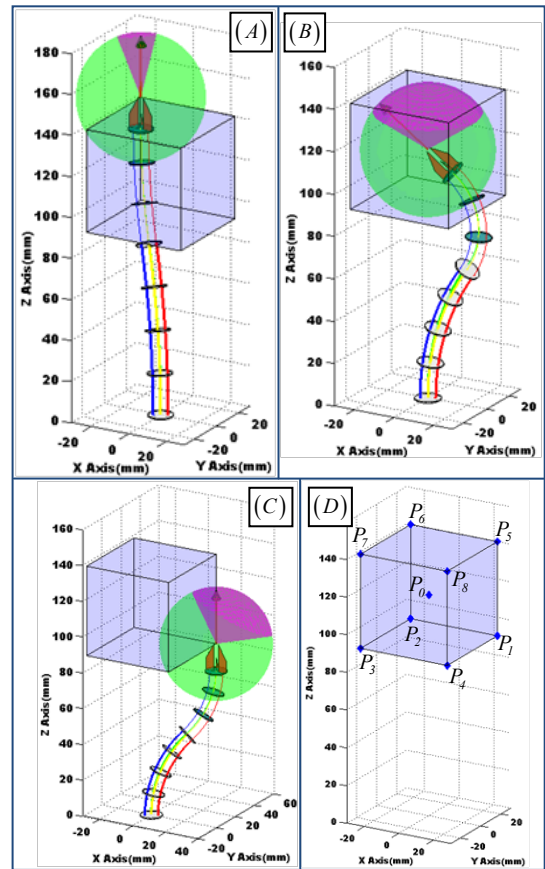


Fig. 11. Distal dexterity evaluated at selected points for Structure C: (A) at  $P_6$  point, (B) at  $P_0$  point, (C) at  $P_1$  point pointing inwards, and (D) shows annotation for all the selected points.

Please note that in Fig. 10(C)-(D), there two disconnected patches. These two disconnected patches can only be reached by driving the tip of the gripper away from and then back to the selected point.

From values presented in Table III, Structure A has an average of 1.236 for the evaluated distal dexterity, while Structure B has an average of 0.658 and Structure C has an average of 1.582. Besides drawing a conclusion that Structure C is more desired, more insights can be observed:

- Distal dexterity at points through  $P_5$  to  $P_8$  is comparable for all the structures because these points are all close to the boundaries of the translational workspace, referring to Fig. 6, Fig. 7 and Fig. 8.
- Distal dexterity at point  $P_0$  is a cap shape for Structure A as in Fig. 9(C) and Structure C as in Fig. 11(B). This is more desired than the strap shape for Structure B as in Fig. 10(B), because the strap shape means surgeons lose the capability of pointing grippers upwards in  $\hat{z}_w$  direction.
- Distal dexterity of Structure C at points through  $P_1$  to  $P_4$  is considerably higher than that of Structure A and Structure B. The essential reason is that these points are substantially further away from the workspace boundaries. Hence, if the functional volume is moved lower in Fig. 8, evaluation of the overall distal dexterity of Structure C would become even better.
- Distal dexterity of Structure C at points through  $P_1$  to  $P_4$  is also of better quality, pointing upwards as in Fig. 11(C).

Grippers of Structure A and Structure B point sideward as in Fig. 9(D) and Fig. 10(D) respectively, which is not desired for surgical manipulation when pulling a tissue from  $P_0$  to  $P_1$  (flipping occurs as pointing direction of grippers have to change considerably).

## VI. CONCLUSION

This paper presented a comparison for distal dexterity among three different structures which all use continuum mechanisms. They could all be potentially applied in surgical robotic systems which use a single access port, such as SPA and N.O.T.E.S surgeries.

Results showed that Structure C, which consists of continuum segments with a varying length, generates the best distal dexterity according to the evaluation criterion proposed in Section II of this paper.

These results could serve as a design reference for future development of surgical robotic slaves. Upon designing robotic arms which use two continuum segments from Fig. 3, instead of incorporating a translational module (Structure A) or adding a third segment (Structure B), design efforts should be made to realize variation of the segments' length (Structure C) with variation ranges as big as possible. Such a structure would not only generate a bigger workspace but also allow surgeons to orient tools more as desired.

## REFERENCES

- [1] G. Navarra, E. Pozza, S. Occhionorelli, P. Carcoforo, and I. Donini, "One-Wound Laparoscopic Cholecystectomy," *British Journal of Surgery*, vol. 84, No.5, p. 695, 1997.
- [2] S. A. Giday, S. V. Kantsevov, and A. N. Kalloo, "Principle and History of Natural Orifice Transluminal Endoscopic Surgery (NOTES)," *Minimally Invasive Therapy and Allied Technologies*, vol. 15, No.6, pp. 373-377, Dec 2006.
- [3] M. F. McGee, M. J. Rosen, J. Marks, R. P. Onders, A. Chak, A. Faulx, V. K. Chen, and J. Ponsky, "A Primer on Natural Orifice Transluminal Endoscopic Surgery: Building a New Paradigm," *Surgical Innovation*, vol. 13, No.2, pp. 86-93, 2006.
- [4] E. D. Flora, T. G. Wilson, I. J. Martin, N. A. O'Rourke, and G. J. Maddern, "A Review of Natural Orifice Transluminal Endoscopic Surgery (NOTES) for Intra-abdominal Surgery: Experimental Models, Techniques, and Applicability to the Clinical Setting," *Annals of Surgery*, vol. 247, No.4, pp. 583-602, April 2008.
- [5] A. A. Gumbs, L. Milone, P. Sinha, and M. Bessler, "Totally Transumbilical Laparoscopic Cholecystectomy," *Journal of Gastrointestinal Surgery*, Aug 2008.
- [6] J. R. Romanelli and D. B. Earle, "Single-Port Laparoscopic Surgery: an Overview," *Surgical Endoscopy*, vol. 23, No.7, pp. 1419-1427, April 2009.
- [7] J. Ding, K. Xu, R. Goldman, P. K. Allen, D. L. Fowler, and N. Simaan, "Design, Simulation and Evaluation of Kinematic Alternatives for Insertable Robotic Effectors Platforms in Single Port Access Surgery," in *IEEE International Conference on Robotics and Automation (ICRA)*, Anchorage, Alaska, USA, 2010, pp. 1053-1058.
- [8] M. Piccigallo, U. Scarfogliero, C. Quaglia, G. Petroni, P. Valdastrì, A. Menciasì, and P. Dario, "Design of a Novel Bimanual Robotic System for Single-Port Laparoscopy," *IEEE/ASME Transaction on Mechatronics*, vol. 15, No.6, pp. 871-878, Dec 2010.
- [9] Y. Sekiguchi, Y. Kobayashi, Y. Tomono, H. Watanabe, K. Toyoda, K. Konishi, M. Tomikawa, S. Ieiri, K. Tanoue, M. Hashizume, and M. G. Fujie, "Development of a Tool Manipulator Driven by a Flexible Shaft for Single Port Endoscopic Surgery," in *IEEE / RAS-EMBS International Conference on Biomedical Robotics and Biomechanics (BIOROB)*, Tokyo, Japan, 2010, pp. 120-125.
- [10] K. Xu, R. E. Goldman, J. Ding, P. K. Allen, D. L. Fowler, and N. Simaan, "System Design of an Insertable Robotic Effector Platform for Single Port Access (SPA) Surgery," in *IEEE/RSJ International Conference on Intelligent Robots and Systems (IROS)*, St. Louis, MO, USA, 2009, pp. 5546-5552.
- [11] A. Yagi, K. Matsumiya, K. Masamune, H. Liao, and T. Dohi, "Rigid-Flexible Outer Sheath Model Using Slider Linkage Locking Mechanism and Air Pressure for Endoscopic Surgery," in *International Conference on Medical Image Computing and Computer-Assisted Intervention (MICCAI)*, Copenhagen, Denmark, 2006, pp. 503-510.
- [12] D. J. Abbott, C. Becke, R. I. Rothstein, and W. J. Peine, "Design of an Endoluminal NOTES Robotic System," in *IEEE/RSJ International Conference on Intelligent Robots and Systems (IROS)*, San Diego, CA, USA, 2007, pp. 410 - 416.
- [13] A. C. Lehman, J. Dumpert, N. A. Wood, L. Redden, A. Q. Visty, S. Farritor, B. Varnell, and D. Oleynikov, "Natural Orifice Cholecystectomy using a Miniature Robot," *Surgical Endoscopy*, vol. 23, No.2, pp. 260-266, Feb 2009.
- [14] N. Simaan, K. Xu, A. Kapoor, W. Wei, P. Kazanzides, P. Flint, and R. H. Taylor, "Design and Integration of a Telerobotic System for Minimally Invasive Surgery of the Throat " *International Journal of Robotics Research*, vol. 28, No.9, pp. 1134-1153, 2009.
- [15] T. Yoshikawa, "Manipulability of Robotic Mechanisms," *International Journal of Robotics Research*, vol. 4, No.2, pp. 3-9, June 1985.
- [16] C. A. Klein and B. E. Blaho, "Dexterity Measures for the Design and Control of Kinematically Redundant Manipulators," *International Journal of Robotics Research*, vol. 6, No.2, pp. 72-83, June 1987.
- [17] J. Angeles and C. S. López-Cajún, "Kinematic Isotropy and the Conditioning Index of Serial Robotic Manipulators," *International Journal of Robotics Research*, vol. 11, No.6, pp. 560-571, 1992.
- [18] E. Berber, K. L. Engle, A. Garland, A. String, A. Foroutani, J. M. Pearl, and A. E. Siperstein, "A Critical Analysis of Intraoperative Time Utilization in Laparoscopic Cholecystectomy," *Surgical Endoscopy*, vol. 15, No.2, pp. 161-165, 2004.
- [19] K. Xu and N. Simaan, "An Investigation of the Intrinsic Force Sensing Capabilities of Continuum Robots," *IEEE Transactions on Robotics*, vol. 24, No.3, pp. 576-587, June 2008.
- [20] K. Xu and N. Simaan, "Intrinsic Wrench Estimation and Its Performance Index of Multi-Segment Continuum Robots," *IEEE Transactions on Robotics*, vol. 26, No.3, pp. 555-561, June 2010.
- [21] B. A. Jones and I. D. Walker, "Kinematics for Multisection Continuum Robots," *IEEE Transactions on Robotics and Automation*, vol. 22, No.1, pp. 43-55, Feb 2006.
- [22] R. J. Webster and B. A. Jones, "Design and Kinematic Modeling of Constant Curvature Continuum Robots: A Review " *International Journal of Robotics Research*, vol. 29, No.13, pp. 1661-1683, Nov 2010.